JOURNAL OF COMPUTATIONAL PHYSICS 105, 58–71 (1993)

Vorticity-Velocity Formulation for Three-Dimensional Steady Compressible Flows

A. ERN AND M. D. SMOOKE

Department of Mechanical Engineering, Yale University, New Haven, Connecticut 06520-2159

Received May 9, 1991; revised May 22, 1992

The vorticity-velocity formulation of the Navier–Stokes equations is extended to the solution of three-dimensional compressible fluid flow and heat transfer problems. The basic governing equations are expressed in terms of three Poisson-like equations for the velocity components together with a vorticity transport equation and an energy equation. The resulting seven coupled partial differential equations are solved by a finite difference method on a single grid and a discrete solution is obtained by combining a steady-state and a time-dependent Newton's method. Once a converged solution is obtained, one of the velocity equations can be removed from the system and replaced by the continuity equation and a "conservative" solution is obtained by using the previous solution as a starting estimate for Newton's method with only a few additional iterations. The numerical procedure is evaluated by applying it to natural and mixed convection problems. The formulation is found to be stable at high Rayleigh numbers and it may be applied to a wide variety of flow and heat transfer problems.

1. INTRODUCTION

The present work's principal aim is to develop a numerical model for the study of momentum and heat transfer phenomena in fluid flows that may arise either from fluid dynamics or combustion problems. In particular, it was motivated by our interest in fluid flow and growth rate uniformity in a chemical vapor deposition reactor. Two important features of such problems have to be accounted for. First, the flow phenomena are highly complex and a full three-dimensional study is necessary for the fluid motion to be properly understood [1, 2]. Due to the large amount of computational time and storage requirements needed in such systems, these problems have often been tackled using a two-dimensional model; the basis for such an assumption being that if one of the cross-stream dimensions of the enclosure is "large" enough, side-wall effects may be neglected. This assumption will not be made in the present work. The second feature of such problems is that, due to large variations in the temperature in the flow domain, the density can vary by as much as a factor of three which implies that compressibility cannot be neglected. In addition, the temperature gradient may result from chemical reactions present in the system. As a consequence, the Boussinesq approximation cannot be made, since the effect of temperature on density may not be confined to the body force term of the momentum equations.

There are three different approaches that have been undertaken to solve the set of Navier–Stokes equations. One approach is the streamfunction-vorticity formulation which has long been used to solve two-dimensional incompressible flow problems [3, 4]. Indeed, in two dimensions, this method is attractive because, first, it eliminates the coupling associated with the presence of the pressure in the momentum equations; second, it reduces the number of equations to be solved by one; and, third, it also has the important advantage that continuity is explicitly satisfied locally. However, the specification of boundary conditions meets with difficulties when one attempts to specify vorticity boundary values. Indeed, the velocity boundary conditions provide two sets of boundary conditions on the streamfunction and none on the vorticity. A boundary condition for the vorticity at the wall in terms of the streamfunction may be derived, for instance, if the vorticity is supposed to vary linearly away from a no-slip wall [4]. A complete account of such boundary conditions and related problems is well documented by Roache [5]. More recently, some new schemes have been developed in which the vorticity boundary conditions are of integral (non-local) type instead of boundary-value (local) type [6]. These integral conditions on the vorticity provide the necessary number of linearly independent equations needed to close the system. These conditions were extended later [7] for time-dependent problems using a method which exhibits vorticity creation on the boundary, leading also to explicit boundary conditions for the vorticity of an integral-differential nature.

In the three-dimensional case, although the existence of the analogue of the streamfunction, referred to as the vector potential, had been known for over a century, its first successful implementation was not achieved until Aziz and

0021-9991/93 $5.00

Hellums [8] solved a natural convection problem using this method. The main reason for such a delay is due mostly to the increased computer storage requirements and to the determination of a set of suitable boundary conditions for the vector potential. Such boundary conditions were first derived for confined flow problems [9] and later extended through the use of an additional scalar potential to account for the through-flow velocities [10]. Some further problems related to this scalar-vector potential formulation are discussed in [11, 12], where it is proposed to introduce an auxiliary solenoidal velocity field instead of the scalar potential. Some recent successful implementations of the vorticity-vector potential formulation include natural convection problems [2] and inlet and indraft wind tunnel simulations [13]. The use of a streamfunction-vorticity transport procedure for three-dimensional external flows has also been reported [14].

Alternatively, numerical methods using primitive variables have been developed and successfully implemented in different geometries of practical interest [15–18]. The popularity of these methods stems primarily from their relatively straightforward extension to three dimensions and to turbulent flows. In the primitive variables formulation, the velocity field is computed using the momentum equations and the pressure field is recovered from the continuity equation. The continuity equation may also be replaced by a Poisson equation for the pressure obtained by taking the divergence of the momentum equations [19] with suitable boundary conditions [20]. As a result of the difference in nature of the governing equations, the discrete pressure field has to be determined in a manner consistent with the discrete continuity equation. This can be achieved to machine zero on a staggered grid. However, staggered mesh schemes do also have drawbacks in complex geometries, in non-orthogonal curvilinear coordinates, and when using complex numerical techniques such as locally adapted grids or multigrid methods [21]. As a consequence, much work has been done recently to develop new computational methods to solve the two-dimensional incompressible Navier–Stokes equations in primitive variables form on a single grid [21–25]. However, the extension of such procedures to three-dimensional compressible cases may still yield some complications.

The third approach that may be adopted, the vorticity-velocity formulation, is a relatively novel formulation which is sometimes called hybrid because it uses variables of both previous methods. Results using the vorticity-velocity formulation have been reported for incompressible flows in both two [26–30] and three dimensions [30–32] and a finite-element formulation for the vorticity-velocity approach has also been presented [33]. In spite of the increased computer storage requirements with respect to the primitive variables approach, this formulation is attractive because it allows replacement of the first-order continuity equation with additional second-order equations, thus allowing an implementation on a single grid. Whereas the streamfunction-vorticity approach also accomplishes the same replacement in two dimensions, the vorticity-velocity formulation can be more easily extended to three dimensions and more accurate local boundary conditions for the vorticity can be derived in a numerically compact way—values of the vorticity on solid boundaries are calculated by means of the derivatives of the velocity. Furthermore, as shown in our numerical experiments, the convective terms in the off-diagonal blocks of the Jacobian matrix, which exert a strong influence in a streamfunction-vorticity approach, disappear.

With an eye towards future applications of practical engineering interest, such as steady-state multidimensional flames and steady-state gas flow simulations inside a chemical vapor deposition reactor, we adopted the vorticity-velocity formulation of the Navier–Stokes equations in the present work. The governing equations are discretized on a single grid so that the numerical method can easily be combined in the near future with multigrid and/or locally adapted grid techniques. In this paper, the formulation of [32] will be extended to the case of three-dimensional, laminar, compressible problems. A potential setback of this formulation is that the pressure is not directly available from the equations. Once the velocity field is obtained, a Poisson equation can be derived for the pressure by taking the divergence of the momentum equations. However, in the low Reynolds number combustion applications in which we are interested, the variations of the pressure may be neglected through the flow domain so that the elimination of the pressure is not critical.

In the next section, the Navier–Stokes and energy equations are transformed into equations for the vorticity, velocity, and temperature and the boundary conditions are discussed. The numerical method is developed in Section 3. Numerical results for natural and mixed convection problems are then presented in Section 4 and compared to previous numerical and experimental work.

2. PROBLEM FORMULATION

2.1. *Governing Equations*

The transport equations defining the conservation of momentum, energy, and continuity have been discussed previously [34]. We restate here the equations of motion and energy for steady laminar flow making the reasonable assumption that viscous dissipation may be neglected. The divergence of a vector is written $\nabla \cdot (\ )$ except for $\nabla \cdot \tau$ which represents the divergence of the tensor τ. The gradient of a scalar quantity is written $\nabla(\ )$.

Continuity,

$$\nabla \cdot (\rho u) = 0, \tag{1}$$

Conservation of momentum,

$$\rho g - \nabla p + \nabla \cdot \tau = \rho (u \cdot \nabla) u, \tag{2}$$

Conservation of energy,

$$\nabla \cdot (k \nabla T) = \rho c_p (u \cdot \nabla) T, \tag{3}$$

where ρ is the density, u is the velocity vector, g is the gravitational acceleration, p is the pressure, τ is the viscous stress tensor, k is the thermal conductivity, and c_p is the specific heat capacity. The viscous stress tensor may be written, while neglecting the bulk viscosity coefficient,

$$\tau_{ij} = \mu \left[\varepsilon_{ij} - \frac{2}{3} \delta_{ij} (\nabla \cdot u) \right], \qquad \varepsilon_{ij} = \frac{\partial u_i}{\partial x_j} + \frac{\partial u_j}{\partial x_i}, \tag{4}$$

where μ is the viscosity and δ_{ij} the identity tensor. We introduce the vorticity vector ζ given by

$$\zeta = \nabla \times u, \tag{5}$$

or in component form

$$\zeta_1 = \frac{\partial u_3}{\partial y} - \frac{\partial u_2}{\partial z}, \qquad \zeta_2 = \frac{\partial u_1}{\partial z} - \frac{\partial u_3}{\partial x}, \qquad \zeta_3 = \frac{\partial u_2}{\partial x} - \frac{\partial u_1}{\partial y}, \tag{6}$$

where $u = (u_1, u_2, u_3)$ and $\zeta = (\zeta_1, \zeta_2, \zeta_3)$.

To form the vorticity transport equation, we take the curl of the momentum equations, which eliminates the pressure gradient term from (2) and we replace the resulting $\nabla \times u$ terms by ζ. This yields the vorticity transport equation in the following form:

$$\begin{aligned} &-\mu \nabla^2 \zeta - \nabla \mu \times [2 \nabla (\nabla \cdot u) - \nabla \times \zeta] \\ &\quad - \nabla \times [\varepsilon \cdot \nabla \mu] - \nabla \rho \times g \\ &\quad + \nabla \rho \times [(u \cdot \nabla) u] + \rho [\nabla \times [\zeta \times u)] = 0. \end{aligned} \tag{7}$$

This equation contains all the first- and second-order derivatives of the viscosity (which may depend on the temperature) and does not involve any approximations. In order to assess the importance of the viscosity derivatives in Eq. (7), we also considered in our numerical experiments the simplified form of the vorticity transport equation,

$$\begin{aligned} &\nabla \times [\mu \nabla \times \zeta] - \nabla \rho \times g \\ &\quad + \nabla \rho [(u \cdot \nabla) u] + \rho [\nabla \times (\zeta \times u)] = 0, \end{aligned} \tag{8}$$

which was derived by neglecting some first-order and all second-order derivatives of the viscosity. This equation has the advantage that it can be easily used in a finite element approach while still keeping some viscosity derivatives and that it only involves second-order derivatives of the vorticity. Finally, since ζ is solenoidal, the term $\nabla \times (\zeta \times u)$ may also be expanded as

$$\nabla \times (\zeta \times u) = (u \cdot \nabla) \zeta - (\zeta \cdot \nabla) u + (\nabla \cdot u) \zeta, \tag{9}$$

so that another possible form of the vorticity transport equation is

$$\begin{aligned} &\nabla \times [\mu \nabla \times \zeta] + \nabla \rho \times [(u \cdot \nabla) u - g] \\ &\quad + \rho [(u \cdot \nabla) \zeta - (\zeta \cdot \nabla) u + (\nabla \cdot u) \zeta] = 0. \end{aligned} \tag{10}$$

In this equation, several dominant physical effects are explicitly represented. Solid boundary walls act as a source (or sink) of vorticity, which is diffused and convected, respectively, by the $\nabla^2 \zeta$ and $(u \cdot \nabla) \zeta$ terms. For three-dimensional flows, the additional term $(\zeta \cdot \nabla) u$ represents the stretching of the vortex lines due to the velocity field and buoyancy forces act through the $\nabla \times \rho$ terms.

Two approaches can be considered to calculate the velocity field. One may treat Cauchy–Riemann (CR) equations for the velocity directly as a system of first-order partial differential equations. The Cauchy–Riemann system satisfied by the velocity field is

$$\begin{aligned} \nabla \times u &= \zeta, \\ \nabla \cdot (\rho u) &= 0, \end{aligned} \tag{11}$$

and its solution uses an iterative scheme in which the solenoidal vorticity field is first obtained using a discrete version of the Helmoltz decomposition theorem [31]. The other possibility is to obtain the velocity field directly from Poisson equations derived by taking the curl of Eq. (5) [26–28, 32]. This second approach is more attractive because the coupled equations for the velocity and vorticity can then be solved simultaneously at each grid point. A set of three Poisson-like equations for each component of the velocity vector is derived by taking the curl of the vorticity and using the continuity equation

$$\begin{aligned} \nabla^2 u &= -\nabla \times \zeta + \nabla (\nabla \cdot u) \\ &= -\nabla \times \zeta - \nabla \left(\frac{u \cdot \nabla \rho}{\rho} \right). \end{aligned} \tag{12}$$

The final set of elliptic equations to be solved is then

$$\nabla^2 u = -\nabla\times\zeta - \nabla\left(\frac{u\cdot\nabla\rho}{\rho}\right),$$

$$\mu\nabla^2\zeta + \nabla\mu\times[2\nabla(\nabla\cdot u) - \nabla\times\zeta] + \nabla\times[\varepsilon\cdot\nabla\mu] \qquad (13)$$
$$= \nabla\rho\times[(u\cdot\nabla)u - g] + \rho[\nabla\times(\zeta\times u)],$$

$$\nabla\cdot(k\nabla T) = \rho c_p(u\cdot\nabla)T.$$

One point of the above formulation deserves particular attention. Although the continuity equation was assumed to be satisfied in the derivation of Eq. (12), it is not explicitly guaranteed as a result of the computation. In fact, considering $\phi = (1/\rho)\nabla\cdot(\rho u)$ one can easily see by taking the divergence of (12) that

$$\nabla^2(\nabla\cdot u) = -\nabla^2\left(\frac{u\cdot\nabla\rho}{\rho}\right) \qquad (14a)$$

or

$$\nabla^2\phi = 0 \qquad (14b)$$

inside the computational domain, so that from the "maximum principle," ϕ should be maximal at a boundary [28]. However, the discrete form of (14) may not hold unless a staggered grid arrangement is used [30]. Since we wanted to discretize the equations on a single grid for the reasons discussed in the Introduction, we developed the following alternative approach. The discretization of Eq. (12), together with the continuity equation (1), leads to an overdetermined set of algebraic equations since there are four equations for only three unknowns. For a given vorticity field, two velocity components could be determined through Eq. (12), whereas the last one could be computed through the continuity equation. Hence, in order to check the consistency of any solution of (13) with the continuity equation (1), we used the following two-step algorithm

Step (i). Solve Eqs. (13),

Step (ii). Once a converged solution is obtained, one of the velocity equations (12) is removed and replaced by the continuity equation.

The choice of the velocity component to be removed may be problem-dependent and, in general, the component which is expected to undergo the most significant changes is removed. The issues related to this second step will be discussed in more detail when numerical results are presented in Section 4.

2.2. *Boundary Conditions*

To complete the specification of Eq. (13), boundary conditions must be applied to all sides of the domain illustrated in Fig. 1. On solid walls, the no-slip condition is enforced on the velocity field by setting

$$u_1 = 0, \qquad u_2 = 0, \qquad u_3 = 0. \qquad (15)$$

If any inflow boundary is present, the velocities are set to the inlet velocities through the use of standard Dirichlet boundary conditions. On any outflow boundary, all normal derivatives are set to zero to simulate fully developed flow. As motivated in [32], the vorticity is computed on no-slip boundaries using Eq. (6), where only the normal velocity derivatives are kept. Assuming the six boundaries S_1 through S_6 shown in Fig. 1 to be no-slip walls, we have

On S_1 and S_6,

$$\zeta_1 = 0, \qquad \zeta_2 = -\frac{\partial u_3}{\partial x}, \qquad \zeta_3 = \frac{\partial u_2}{\partial x},$$

On S_2 and S_5,

$$\zeta_1 = \frac{\partial u_3}{\partial y}, \qquad \zeta_2 = 0, \qquad \zeta_3 = -\frac{\partial u_1}{\partial y}, \qquad (16)$$

On S_3 and S_4,

$$\zeta_1 = -\frac{\partial u_2}{\partial z}, \qquad \zeta_2 = \frac{\partial u_1}{\partial z}, \qquad \zeta_3 = 0.$$

For inflow boundaries, the inlet vorticity should incorporate two terms. The first one is the vorticity brought in by the entering gas and the second one takes into account the velocity field inside the domain and is computed using inward normal derivatives of the velocity at the inlet, given by (16). The boundary conditions on the temperature are, in

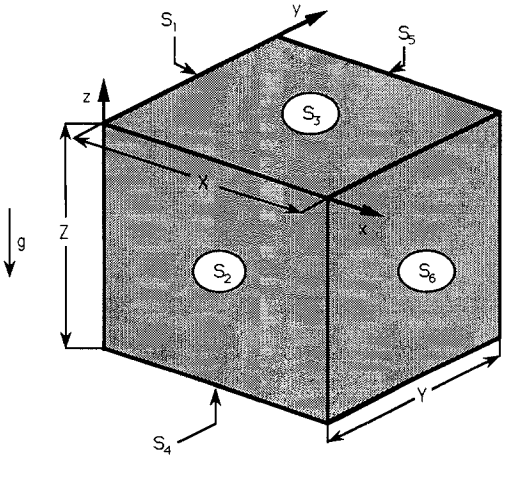

FIG. 1. The solution region and coordinate orientation; indices for opposite boundaries sum up to seven.

comparison, simpler. We may either specify the temperature or the heat flux at a surface, thereby imposing a Dirichlet or a Neumann boundary condition on the temperature.

3. METHOD OF SOLUTION

Our goal is to obtain a discrete solution of the governing equations on a three-dimensional tensor-product mesh $\mathcal{M}$ with elements whose sides are parallel to the x, y, and z directions. Since the flow phenomena often exhibit recirculation effects, there may not be any direction in the flow domain for which the velocity component is always positive or zero. Hence, the governing equations are elliptic and a numerical iterative procedure must be employed for their solution. Computationally, we combine a steady-state and a time-dependent solution method. The time-dependent approach is used to help obtain a converged numerical solution which will then be used as a starting estimate for the steady-state solution procedure.

3.1. *Finite Difference Approximations*

The set of governing equations and the boundary conditions are discretized using finite difference approximations. Mesh point variables are typically denoted by $\phi^{i,j,k}$ but arguments are omitted when they have their default value i, j, or k; thus $\phi^{i-1}=\phi^{i-1,j,k}$. In the following presentation, we will assume the mesh to be uniform. The restriction is not necessary but it simplifies considerably the notation. Standard central differences are used throughout for the first- and second-order derivatives, except for the convective terms for which upwind differences may be used. Upon introducing the notation

$$\delta_x\phi=\frac{\phi^{i+1/2}-\phi^{i-1/2}}{\Delta x},\qquad v_x\phi=\frac{\phi^{i+1/2}+\phi^{i-1/2}}{2}, \tag{17}$$

first-order and second-order derivatives are discretized by

$$\left(\frac{\partial\phi}{\partial x}\right)^i=\delta_x v_x\phi=\frac{\phi^{i+1}-\phi^{i-1}}{2\Delta x},\qquad \left(\frac{\partial^2\phi}{\partial x^2}\right)^i=\delta_x\delta_x\phi=\frac{\phi^{i+1}-2\phi^i+\phi^{i-1}}{\Delta x^2}. \tag{18}$$

The definition of the operators δ_y, δ_z, v_y, v_z is similar. If the second derivative terms include a coefficient a, the discretization is given by

$$\begin{aligned}\frac{\partial}{\partial x}\left(a\frac{\partial\phi}{\partial x}\right)&=\delta_x(v_x(a)\,\delta_x(\phi))\\&=\frac{1}{2\Delta x^2}((a^{i+1}+a^i)(\phi^{i+1}-\phi^i)\\&\quad-(a^i+a^{i-1})(\phi^i-\phi^{i-1})),\end{aligned} \tag{19}$$

whereas for cross derivatives we have

$$\begin{aligned}\frac{\partial}{\partial x}\left(a\frac{\partial\phi}{\partial y}\right)&=\delta_x v_x\{a\delta_y v_y(\phi)\}\\&=\frac{1}{4\Delta x\,\Delta y}(a^{i+1,j}(\phi^{i+1,j+1}-\phi^{i+1,j-1})\\&\quad-a^{i-1,j}(\phi^{i-1,j+1}-\phi^{i-1,j-1})).\end{aligned} \tag{20}$$

If the continuity equation is used for one of the velocity components, say u_3, the first two terms are discretized with centered differences and the last one using upwind differences

$$\delta_x v_x(\rho u_1)+\delta_y v_y(\rho u_2)+\frac{\rho^k u_3^k-\rho^{k-1}u_3^{k-1}}{\Delta z}=0, \tag{21}$$

where the upwind difference is used to increase the efficiency of the linear algebra solution method.

For the vorticity boundary conditions, the normal derivatives on the wall are discretized with a first-order backward or forward difference. Rather than introducing the velocities at a distance $2h$ from the wall, the vorticity at a distance h from the wall is used [32]. For instance, at the top wall S_3 shown in Fig. 1, corresponding to $z=k$, we have

$$\zeta_1^k=\frac{2}{h}u_2^{k-1}-\zeta_1^{k-1},\qquad \zeta_2^k=-\frac{2}{h}u_1^{k-1}-\zeta_2^{k-1},\qquad \zeta_3^k=0. \tag{22}$$

3.2. *Newton's Method*

In the previous section, the problem of finding an analytic solution to the set of governing equations (13) was converted into one of finding an approximation to this solution at each point (x_i, y_j, z_k) of the mesh. Hence, with the finite difference equations written in residual form, we seek the solution of the system of nonlinear equations,

$$F(U)=0. \tag{23}$$

The system in (23) is solved by Newton's method, which has been proven to be an efficient tool to solve strongly coupled sets of equations [35]. This leads to the iterations

$$J(U^n)(U^{n+1} - U^n) = -\lambda^n F(U^n), \qquad n = 0, 1, 2, \ldots, \tag{24}$$

where $J(U^n) = \partial F(U^n)/\partial U$ is the Jacobian matrix and λ^n is the nth damping parameter [36]. Newton's method will converge, providing that the starting estimate U^0 is sufficiently close to $\hat{U}$, the solution of (23). The Newton iterations continue until the size of $\|U^{n+1} - U^n\|_2$ is reduced beyond a given tolerance (typically 10^{-6}).

We anticipate that the formation of the Jacobian and its factorization will account for a considerable part of the cost of the numerical method. Therefore, a modified Newton's method is used in which the Jacobian is re-evaluated only periodically, according to whether the rate of convergence is fast enough. The rate of convergence is tested as described in [37]. If it is too slow, we use new Jacobian information, whereas if it is acceptable, we continue performing modified Newton iterations.

3.3. *Linear Algebra*

The Jacobian matrix is evaluated numerically rather than analytically. We form several columns of the Jacobian simultaneously, using vector function evaluations where all the i, j, k nodes of the mesh corresponding to the same value of the parameter

$$\alpha = (i + 3j + 9k) \bmod 27 \tag{25}$$

are perturbed simultaneously [38]. Once the Jacobian is formed, the resulting linear system is solved using a block-line SOR method. One of the three grid line directions, say x, is chosen for a direct solution method using an efficient block-tridiagonal matrix algorithm. SOR iterations are performed along the two remaining directions. The choice of the line direction may be problem-dependent and, in general, it is guided by the fact that for a direct inverse matrix algorithm, the values of the solution along the chosen lines are immediately affected by the values at the two opposite boundaries connected by the grid lines. A block-plane matrix algorithm could also have been used, but it would have required the partial fill-in of the Jacobian, which was not desirable from a storage point of view.

We point out that the spatial discretization used in forming (23) leads to a Jacobian matrix which can be written in a block 19 diagonal form. We denote by $U^{i,j,k}$ the vector formed by the seven unknowns $(u_1, u_2, u_3, \zeta_1, \zeta_2, \zeta_3, T)$ at node i, j, k and by $F^{i,j,k}$ the array formed by the seven derivatives are present in the equations, only the seven block-diagonals,

$$\frac{\partial F^{i,j,k}}{\partial U^{i,j,k}}, \quad \frac{\partial F^{\pm i,j,k}}{\partial U^{i,j,k}}, \quad \frac{\partial F^{i,\pm j,k}}{\partial U^{i,j,k}}, \quad \frac{\partial F^{i,j,\pm k}}{\partial U^{i,j,k}}, \tag{26}$$

are nonzero in the Jacobian matrix, whereas if cross derivatives are present, the following 12 block-diagonals are also nonzero

$$\frac{\partial F^{\pm i,\pm j,k}}{\partial U^{i,j,k}}, \quad \frac{\partial F^{\pm i,j,\pm k}}{\partial U^{i,j,k}}, \quad \frac{\partial F^{i,\pm j,\pm k}}{\partial U^{i,j,k}}. \tag{27}$$

We point out that cross derivatives appear in the equations only through the density in Eq. (12) so that the off-diagonal entries (27) may be considered as "perturbations" of the full Jacobian. Hence, one expects Newton iterations still to converge if they are performed using a "partial" Jacobian formed only with the seven block-diagonals given by (26) and incorporating none of the entries listed in (27). This procedure ultimately leads to the same solution as from (14), since only the iteration matrix has been changed in the procedure. Its potential setback may be a slower convergence rate and more iterations may be needed to obtain a converged solution. But, on the other hand, it alleviates considerably the computer storage requirements, so that finer grids can be used. The procedure to evaluate the Jacobian can be further simplified as follows. Instead of splitting the mesh nodes into 27 independent groups, we perturb simultaneously all the i, j, k nodes that correspond to the same value of the parameter $\beta = (i + 2j + 3k) \bmod 7$ and thereby form an "approximate partial" Jacobian. While this procedure obviously shares the same potential risks as the previous one, the "approximate partial" Jacobian requires much less CPU time to be evaluated since the perturbed residual (23) in vector form is computed only seven times. Obviously, the optimal strategy for the evaluation of the Jacobian matrix may be problem dependent and a complete discussion of its applications to general elliptic systems is beyond the scope of this paper. In both test problems considered in Section 4, Newton's method was found to be fairly insensitive to the neglected off-diagonal terms, due to the Poisson-like form of the seven governing equations. These aspects will be further discussed in Section 4.

3.4. *Pseudo-Transient Iterations*

We apply a pseudo-transient iteration to bring the starting estimate into the convergence domain of Newton's method. The original nonlinear elliptic problem is cast into

to the left-hand side of (23) [2]. For the internal nodes, a fully implicit transient scheme is employed by solving

$$\mathscr{F}(U^{n+1}) = F(U^{n+1}) + \frac{U^{n+1} - U^n}{\tau^{n+1}} = 0, \qquad (28)$$

where for a function $\phi(t)$, we define $\phi^n = \phi(t^n)$ and where the time step is $\tau^{n+1} = t^{n+1} - t^n$. At each transient iteration, we solve system (28) using again the modified Newton's method, the main difference being that the diagonal of the Jacobian is weighted by the quantity $1/\tau^{n+1}$. Thus, the resulting linear system can be made diagonally dominant by an appropriate choice of τ^{n+1} and only a few SOR iterations are needed for its solution. We also point out that the transient iterations will yield a numerical solution procedure that is in general less sensitive to the initial starting estimate than if Newton's method were applied directly. Hence, when the steady-state equations are ultimately solved, only a few additional Newton iterations are needed to obtain the numerical solution.

It should be mentioned that any attempt to use the continuity equation instead of one of the elliptic velocity equations starting with an initial guessed solution did not meet with any success. On the contrary, once a converged numerical solution of (13) is obtained, one of the velocity equations is removed and replaced by the continuity equation. Newton's method can be applied successfully to this new set of equations and only a few more iterations are needed to get the final solution. In fact, we believe that the convergence domain of Newton's method $\mathscr{D}$ is much smaller if the continuity equation is used and hence the solution has to be brought into $\mathscr{D}$ by solving first the fully elliptic system (13).

4. RESULTS AND DISCUSSION

In this section, we apply the vorticity-velocity formulation and the computational method discussed in Section 3 to three-dimensional natural and mixed convection problems. All the physical properties have been considered as temperature-dependent and have been computed using the procedures discussed in [39] for a hydrogen flow. The density was computed using the perfect gas law, assuming the pressure to be constant. All the computations were carried out on a Multiflow Trace 14/300 computer and on an IBM RS6000 Model 550 for the fine $41 \times 41 \times 41$ grid computations requiring up to 260 Mb of work space. Typically, 100 unsteady iterations and 5 to 10 steady Newton iterations were required to solve the problems. CPU times varied from one to six hours.

4.1. *Double-Glazed Window Problem*

Referring to Fig. 1, we considered a cavity enclosed by six impermeable boundaries, where the four planes S_1, S_3, S_4, and S_6 are adiabatic and a temperature gradient is imposed through the two boundaries normal to the y-direction

$$\begin{aligned} &\text{on } S_2, \quad T = T_1, \\ &\text{on } S_5, \quad T = T_0. \end{aligned} \qquad (29)$$

Except if mentioned explicitly, all the boundaries are stationary and the fluid motion is caused solely by the buoyancy effects and a vortex normal to the x-direction is expected to develop inside the cavity. In presenting our numerical results, we will assume that the origin of the three coordinate axes is the center of the cavity. Further, any section of the cavity perpendicular to the x, y, or z-direction will be called an x, y, or z-section, respectively.

For natural convection problems, the motion of the gas can be characterized by two dimensionless numbers, the Prandtl number and the Rayleigh number,

$$\mathrm{Pr} = \frac{c_p \mu}{k}, \qquad \mathrm{Ra} = \frac{\rho^2 g D^3 c_p \Delta T}{\mu k T}, \qquad (30)$$

where c_p is the heat capacity at constant pressure, μ is the viscosity, k is the thermal conductivity, ρ is the density, g is the gravitational acceleration, D is a reference dimension, T is a reference temperature, and $\Delta T = T_1 - T_0$ is the temperature difference between the hot and cold walls. The reference dimension in this case is Y, the distance between the two isothermal walls. The two aspect ratios X/Y and Z/Y were taken equal to unity. In our computations, a Prandtl number of 0.67 was obtained, which is a typical value for gases; the two isothermal walls were kept at $T_0 = 300$ K and $T_1 = 1000$ K (except for the use of the Boussinesq approximation where $T_1 = 400$ K) and the cavity size was taken to be $Y = 8$ cm. The Rayleigh number varied between 10^2 and 10^6 by changing the pressure inside the cavity; the typical resulting pressure values ranged between 0.1 and 1.0 atm.

In order to assess the quantitative accuracy of the developed algorithm, we compared our results to previous numerical experiments in two dimensions [28, 40]. We set the hot wall temperature at 400 K, assumed the physical properties to be temperature-independent and made the Boussinesq approximation. In order to simulate a two-dimensional flow, we imposed that all normal derivatives vanish on the boundaries normal to the x-direction S_1 and S_6. The velocity profiles at the vertical and horizontal mid-sections are presented in Fig. 2 for $\mathrm{Ra} = 10^4$ and the agreement with the location and amplitude of the maximum velocities as given in [28, 40] appears to be very good. We also compared in Fig. 2 the numerical solutions on a $21 \times 21 \times 21$ and a finer $41 \times 41 \times 41$ grid to verify the grid independence of the results.

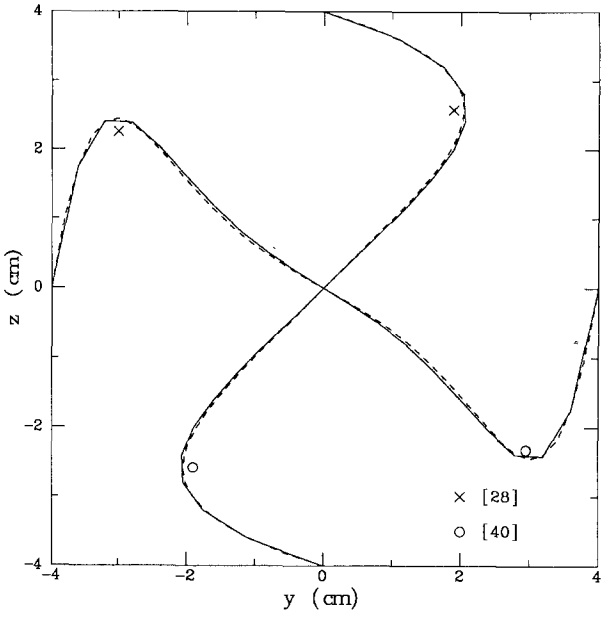

FIG. 2. Profiles of u_2 and u_3 along the vertical and horizontal mid-section at $x=0$ for $\mathrm{Ra}=10^4$ (Boussinesq approximation) on the $21\times21\times21$ (—) and $41\times41\times41$ (– –) grids.

The vorticity-velocity formulation was then evaluated on a mixed convection problem where the gas motion was driven by buoyancy effects as well as by vorticity generation on the sliding top wall S_3. For this problem, the Reynolds number is defined as

$$\mathrm{Re}=\frac{\rho u_0 D}{\mu}, \tag{31}$$

where $-u_0$ ($u_0>0$) is the velocity of the moving top wall. Our two- and three-dimensional results are compared in Fig. 3 with those in [28] for the case $\mathrm{Gr}/\mathrm{Re}^2=0.5$, where the Grashoff number Gr is defined by $\mathrm{Gr}=\mathrm{Ra}/\mathrm{Pr}$. The agreement again appears to be very good and the motion at the mid x-section is fairly well represented by the two-dimensional model.

For the remaining part of this section, we discard the Boussinesq approximation and turn to the solution of the full set of governing equations (13), using a compressible three-dimensional model with temperature-dependent physical properties. The hot wall was kept at 1000 K and we will discuss the results for a Rayleigh number of 10^4 and 10^5, respectively. With the large variations in temperature inducing significant changes of the physical properties and prohibiting the use of the Boussinesq approximation, there is no symmetry in the y-direction and the center of the vortex is shifted towards the cold wall and slightly towards the bottom wall. As a result from our computations, the solution is still symmetric in the x-direction. We also checked the importance of artificial numerical viscosity by discretizing the convective terms with centered or upwind differences and comparing the resulting numerical solutions. No significant differences were encountered. We also compared the various forms of the vorticity transport equation as discussed in Section 2. Whereas the use of (8) can predict accurately the motion in the x-sections, some slight differences may be found in the first component of the velocity u_1 when $\mathrm{Ra}=10^5$, because it is smaller in magnitude. However, no significant changes appeared when expanding the term $\nabla\times(\zeta\times u)$ in (8) as in (10). Finally, we also checked the grid independence of the numerical solution by comparing the results obtained on a $21\times21\times21$ and a finer $41\times41\times41$ grid. For all Rayleigh numbers considered, we found very good agreement as can be seen in Fig. 4 for $\mathrm{Ra}=10^5$.

Some aspects related to the numerical method are discussed next. We first checked the different strategies for evaluating the Jacobian matrix in the case of a Rayleigh number equal to 10^4. Obviously, the optimal choice for the degree of approximation in the Jacobian matrix may be problem-dependent and a complete discussion of the application of Newton's method to nonlinear elliptic systems is beyond the scope of this paper. However, we want to point out through the study of a relatively "hard" test problem that, although cross derivatives are present in the set of governing equations, they might not have to be taken into account in the Jacobian matrix, thus alleviating considerably the computer storage requirements. The converged solution for $\mathrm{Ra}=5000$ was used as a starting estimate and the residual norm is plotted in Fig. 5 versus CPU time for the three strategies discussed in Section 3. A factor of two increase in speed is achieved, if instead of forming a full 19 diagonal Jacobian, a seven diagonal

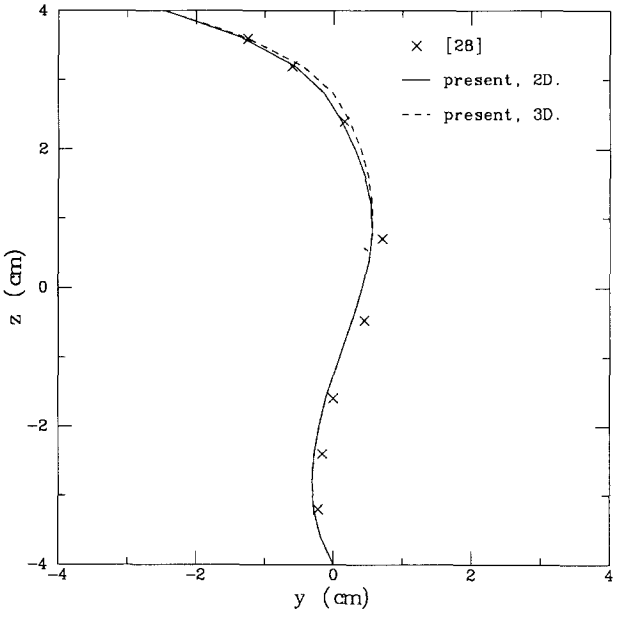

FIG. 3. Profile of u_2 at ($x=0$, $y=0$) for $\mathrm{Ra}=10^4$ and $\mathrm{Gr}/\mathrm{Re}^2=0.5$ (driven-cavity problem).

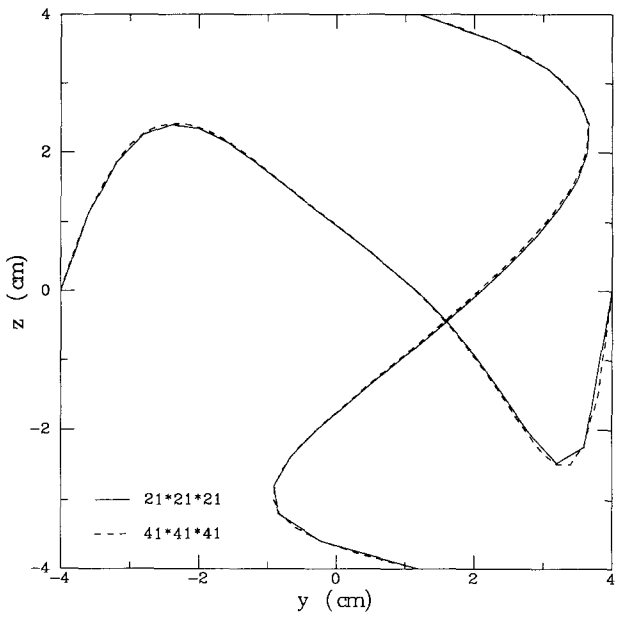

FIG. 4. Mesh refinement check for $Ra = 10^5$ (natural convection).

Jacobian is formed with only seven vector function evaluations. In this case, Newton's method is fairly insensitive to the neglected off-diagonal terms. If a streamfunction-vorticity formulation had been used instead, cross derivatives would also have appeared in the convective terms of the vorticity and energy equations, and such approximations in the Jacobian matrix might have proven to have a more critical effect on the convergence of Newton's method.

Three-dimensional velocity fields have been obtained for various cross sections of the cavity for the cases of $Ra = 10^4$ and 10^5. The results for $Ra = 10^4$ are shown in Fig. 6 for the three mid x, y, and z-sections. Except for x-sections near the lateral boundaries, the same vortex profile was found on all also that the flow is coming up at $y = 0.8$ cm and down at $y = 1.6$ cm as one moves closer to the cold wall. Temperature contour levels for $Ra = 10^4$ are shown in Fig. 8 for the mid x-section and they are qualitatively similar to those obtained in [2, 28]. The three-dimensional motion appears to have little effect on the temperature, since the isotherms almost overlap each other for various x-sections.

The continuity equation can be checked for any numerical solution by computing the nondimensional quantity $\phi = \nabla \cdot (\rho u)$ in the flow domain. Contour levels are presented for ϕ in Fig. 9 for the mid x-section in the case of $Ra = 10^4$ as well as for $\psi = \nabla \cdot \zeta$. The quantities ϕ and ψ were found to be maximal on the boundaries S_2 and S_5. As discussed in Section 2, the numerical solution of (13) can then be used as a starting estimate for solving (23), where the second velocity component equation is removed and replaced by the continuity equation. In all cases, the new solution is obtained on a single grid with only two or three additional Newton iterations. No relevant differences were found between both solutions at all Rayleigh numbers considered and the velocity profiles obtained on the cavity sections with and without the continuity equation overlapped. The same conclusion holds for the heat transfer and temperature predictions which also coincided for both solutions.

The local Nusselt number ($Nu(z)$) distributions along the hot and cold wall are shown in Fig. 10. They were computed using a dimensionless temperature gradient averaged along the x-direction at the heat-transfer surfaces S_2 and S_5 [34]. The nondimensional temperature was $\hat{T} = (T - T_0)/(T_1 - T_0)$. The local Nusselt number distributions were qualitatively the same as those obtained in [28] for two-dimensional models. The profiles for the hot and cold walls

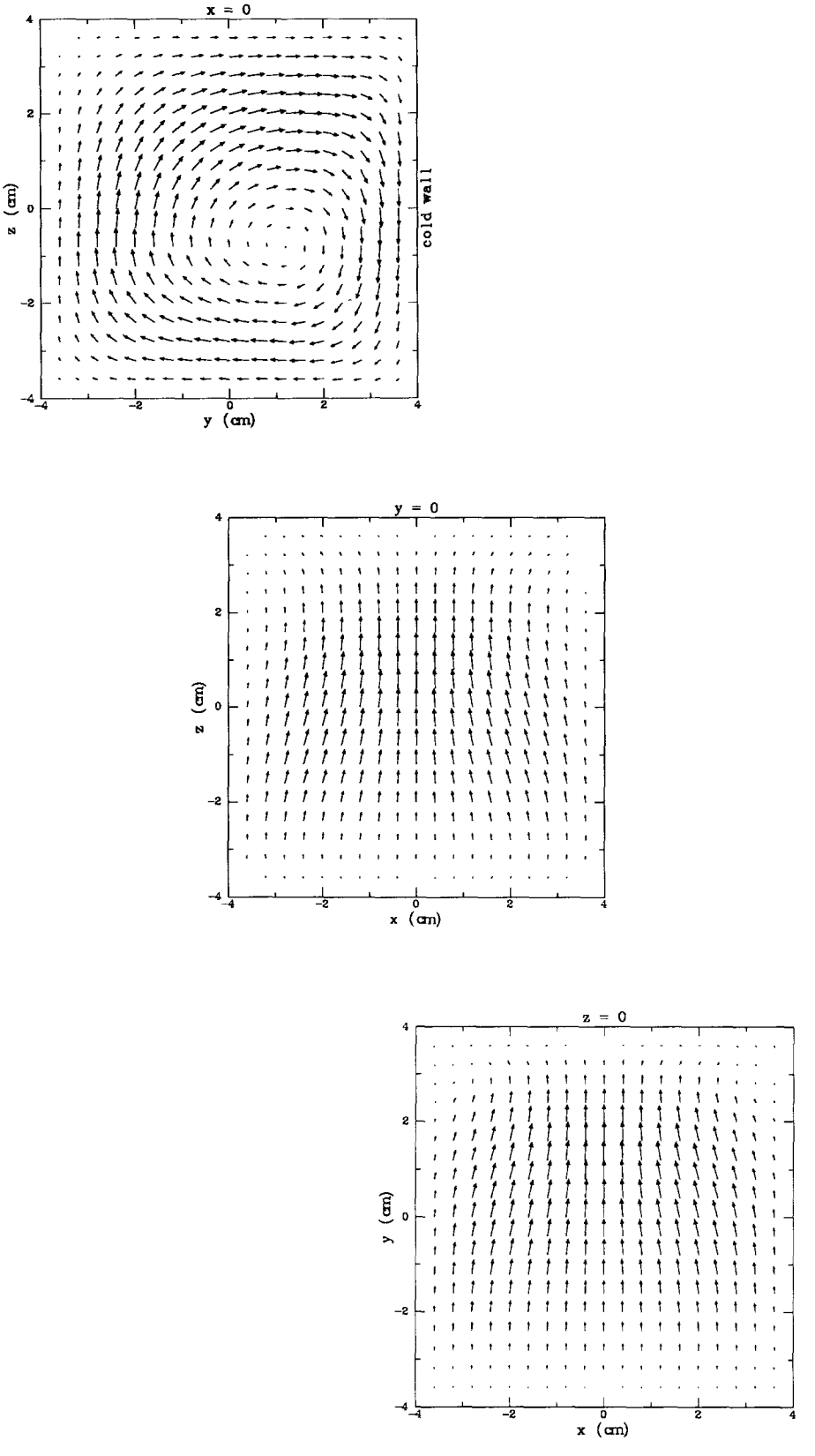

FIG. 6. Velocity fields at various cross-sections for $Ra = 10^4$ solved with a $21 \times 21 \times 21$ equispaced mesh; (a) mid x-section; (b) mid y-section; c) mid z-section.

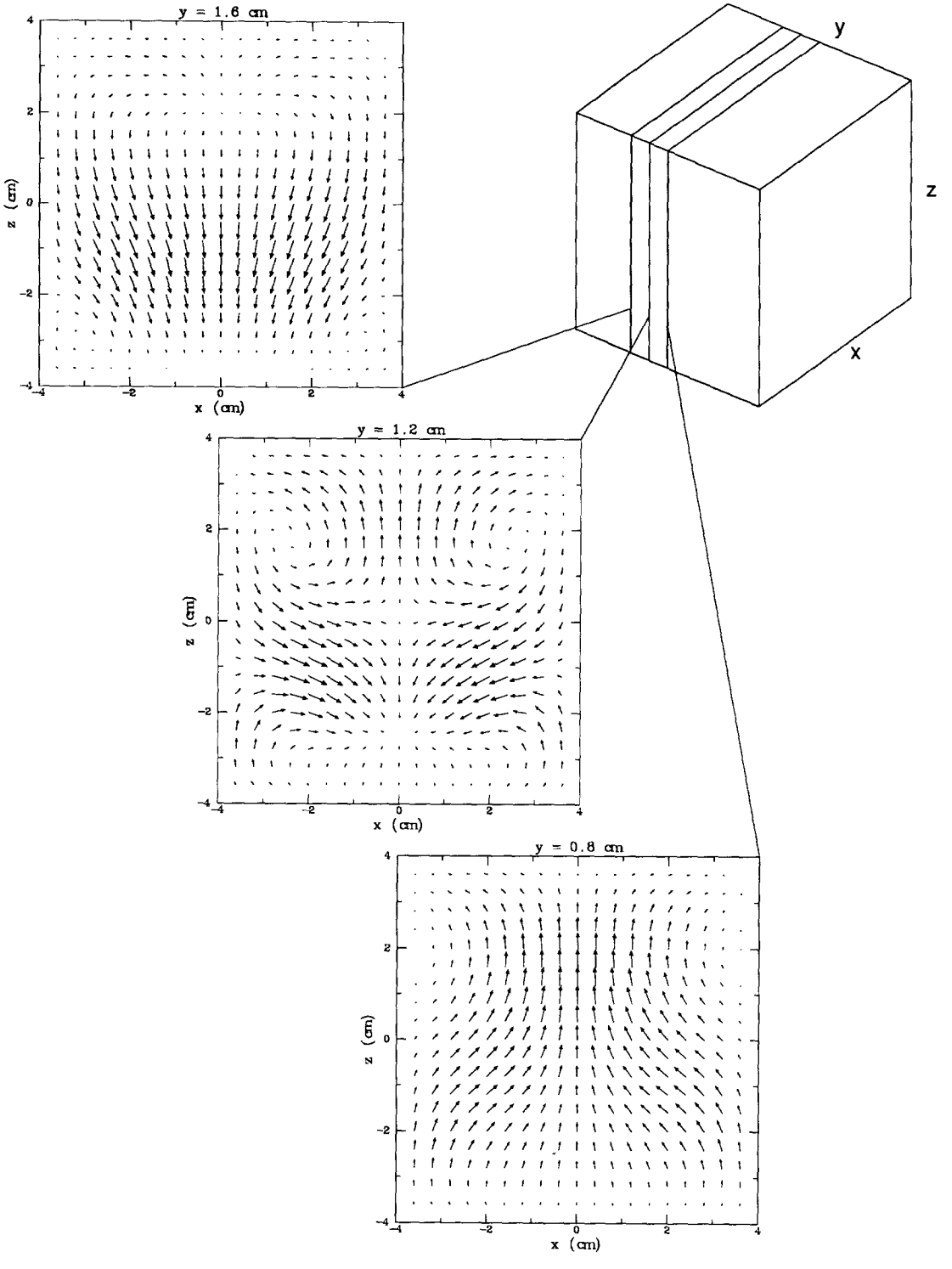

FIG. 7. Velocity fields at three consecutive y-sections for $\mathrm{Ra} = 10^5$ (natural convection).

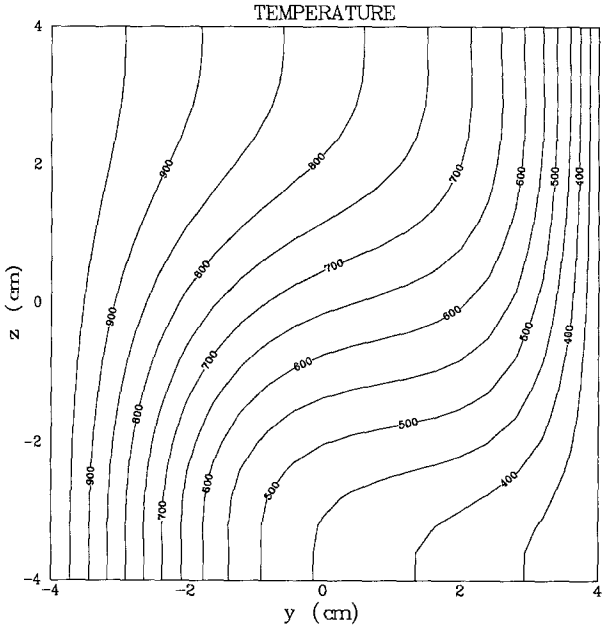

FIG. 8. Isotherms for $Ra = 10^4$ at the mid x-section (natural convection).

are not symmetric with respect to z as opposed to [28]. The local Nusselt numbers are higher for the cold wall because the center of the vortex is nearer the cold wall and higher gradients are expected to develop in that region. The vertically averaged Nusselt numbers obtained for each x-section were compared to the results of [2]. Even though the study in [2] was for a cavity with a transverse aspect ratio of five, the results were still found to be in good agreement.

4.2. *Mixed-Convection Problems*

A chemical vapor deposition (CVD) reactor is studied next as a model for mixed-convection problems. A model for such a reactor is shown in Fig. 11. We assume that a fully developed flow at temperature T_0 enters the reactor at $x = 0$. The outflow boundary is located at $x = X$ and the four other sidewalls S_2, S_3, S_4, and S_5 are no-slip boundaries. The sidewalls S_2 and S_5, normal to the y-direction, are adiabatic boundaries. The top wall S_3 is kept at temperature T_0, thus simulating the case of water cooling. On the lower wall S_1, a heated susceptor at temperature $T_1 = 1000$ K is set up in the second half of the reactor ($x \geqslant X/2$) and a heatup zone before the susceptor is simulated using a linearly ramped temperature profile for $X/4 < x \leqslant X/2$.

As discussed in [41], the controlling numbers for the fluid flow are the Grashof number Gr and the Reynolds number Re given by

$$\mathrm{Gr} = \frac{\mathrm{Ra}}{\mathrm{Pr}}, \qquad \mathrm{Re} = \frac{\rho v_0 D}{\mu}, \tag{32}$$

where v_0 represents the average inlet gas velocity and D, a reference dimension, is the height of the reactor Z. Results for our numerical model will be presented for $Z = 2$ cm and the two aspect ratios X/Z and Y/Z are equal to four and three, respectively. The flow domain was discretized using a $31 \times 21 \times 16$ uniform mesh. Further, an "approximate partial" Jacobian has been used in the solution procedure and no difficulties in the convergence of Newton's method were encountered.

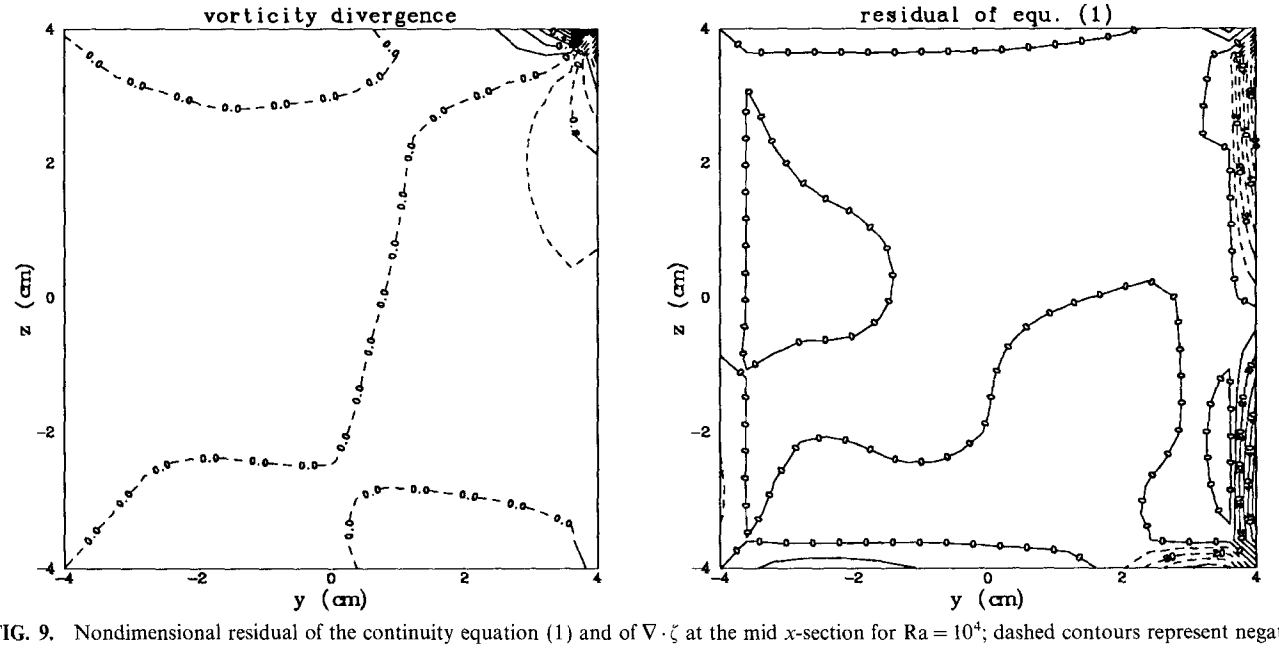

FIG. 9. Nondimensional residual of the continuity equation (1) and of $\nabla \cdot \zeta$ at the mid x-section for $Ra = 10^4$; dashed contours represent negative levels (natural convection).

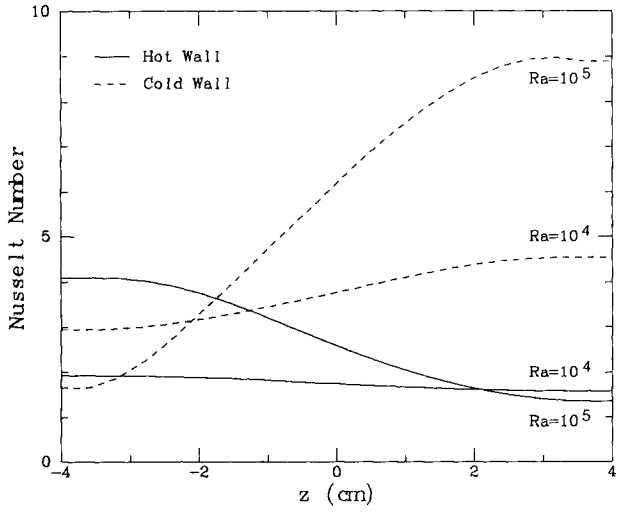

FIG. 10. Local Nusselt number distributions $Nu(z)$ at the hot and cold walls for various Rayleigh numbers (natural convection).

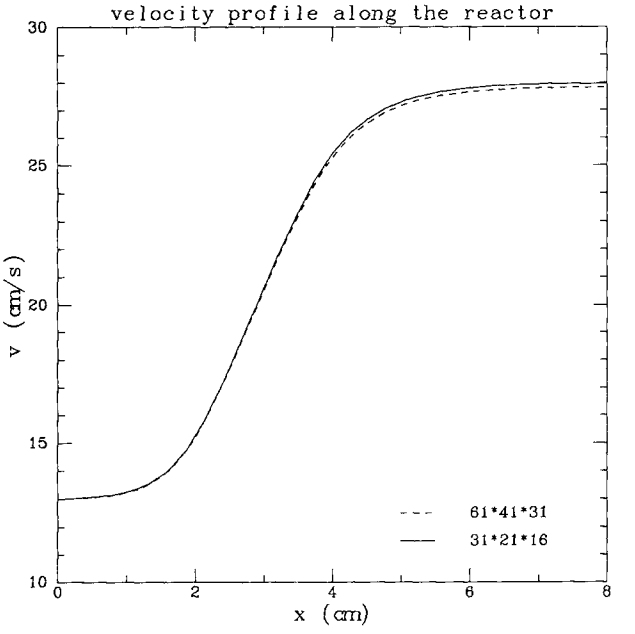

FIG. 12. Velocity profile along the reactor obtained on the coarse and fine grids for Ra = 10 and Re = 1; (mixed convection).

Typical Rayleigh numbers for CVD reactor models are not larger than 10^3, since recirculation in the form of Bénard cells occurs for $\mathrm{Ra} \geqslant 1700$ [41]. Results are presented here in the case of $\mathrm{Ra} = 10$ and $\mathrm{Re} = 1$. The origin of the axes is the center of the inlet boundary S_1. The variation of the longitudinal velocity component u_1 is shown in Fig. 12. One can see that this quantity is multiplied by a factor of two through the heatup zone and then increases only very slightly above the suspector area. Further, as a grid refinement check, we also plot in Fig. 12 the numerical results obtained on a $61 \times 41 \times 31$ grid obtained by doubling the number of grid points in each spatial direction and the agreement is found to be very good. Three-dimensional effects are present in the flow field through the existence of two symmetric longitudinal rolls spinning around the x-axis above the susceptor region. Figure 13 shows the velocity profiles at three cross-stream sections computed using Eq. (7) for the vorticity transport equation. When considering the simplified vorticity transport equation (8) instead of (7) in (13), we found some slight differences in the transverse velocity profiles but the resulting solution lay in the convergence domain of the steady Newton's method for the

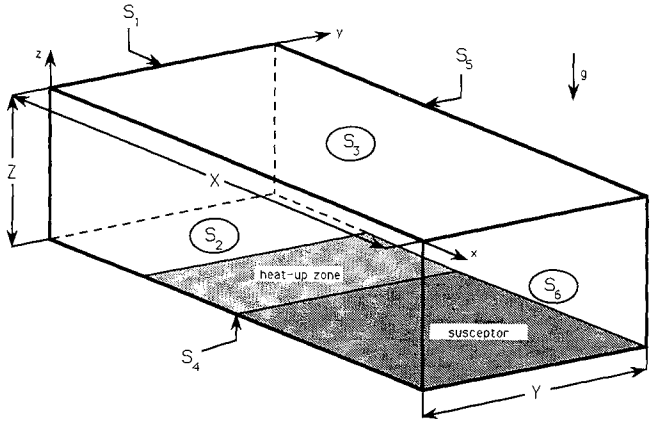

FIG. 11. Computational model for a Chemical Vapor Deposition (CVD) reactor (mixed convection problem); indices for opposite boundaries sum up to seven.

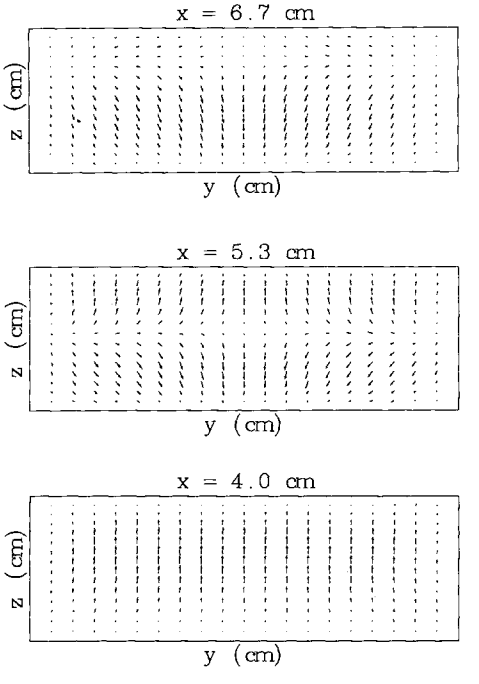

FIG. 13. Velocity fields at various cross-stream sections; Ra = 10 and Re = 1; (mixed convection).

full set of Eqs. (13). Finally, one can see that the vertical component of the velocity u_3 tends to be negative on the symmetry plane $y = 0$; the same result was found in [42] for a similar reactor model with adiabatic sidewalls.

The continuity equation residual in nondimensional form was again checked for every converged solution. In all cases, we found that mass balances were satisfied within 1%. The residual reached its maximum value at the beginning of the heatup zone and then decreased along the susceptor. It also increased near the outflow boundary due to the inaccuracy of the outlet boundary condition, which assumed the flow to be fully developed. As for natural convection problems, mass balances were satisfied for the final conservative solu-

3. J. E. Fromm, Report No. 2910, Los Alamos Scientific Laboratory, Los Alamos, New Mexico, 1963 (unpublished).
4. A. D. Gosman, W. M. Pun, A. K. Rundal, D. B. Spalding, and M. Wolfstein, *Heat and Mass Transfer in Recirculating Flows* (Academic Press, New York, 1969).
5. P. J. Roache, *Computational Fluid Dynamics* (Hermonsa, Albuquerque, NM, 1972).
6. L. Quartapelle, *J. Comput. Phys.* **40**, 453 (1981).
7. C. R. Anderson, *J. Comput. Phys.* **80**, 72 (1989).
8. K. Aziz and J. D. Hellums, *Phys. Fluids* **10**, 314 (1967).
9. G. J. Hirasaki and J. D. Hellums, *Quart. Appl. Math.* **26**, 331 (1968).
10. G. J. Hirasaki and J. D. Hellums, *Quart. Appl. Math.* **28**, 293 (1970).
11. A. K. Wong and J. A. Reizes, *J. Comput. Phys.* **55**, 98 (1984).
12. O. R. Tutty, *J. Comput. Phys.* **64**, 368 (1986).

a couple of additional Newton iterations on a single gri , and the seven solution fields of both solutions were again found to overlap.

14. R. L. Davis, J. E. Carter, and M. Hafez, *AIAA J.* **27**, 892 (1989).
15. V. Pratap and D. Spalding, *Int. J. Heat Mass Transfer* **19**, 1183 (1976).
16. J. H. Pulliam and J. L. Steger, *AIAA J.* **18**, 159 (1980).
17. Y. N. Xu and M. D. Smooke, *J. Comput. Phys.*, in press.